– Supporting Information –

Excitation of Strong Localized Surface Plasmon Resonances in Highly Metallic Titanium Nitride Nano-Antennas for Stable Performance at Elevated Temperatures

Mena N. Gadalla[*,†], *Andrew S. Greenspon*[†], *Michele Tamagnone*[†], *Federico Capasso*[†], *Evelyn L. Hu*[†]

[†]John A. Paulson School of Engineering and Applied Sciences, Harvard University, Cambridge, Massachusetts 02138, United States

* E-mail address: mgadalla@g.harvard.edu

1. TiN thin film deposition and characterization:

The TiN thin films were reactively sputtered using 2" diameter titanium (Ti) target while flowing Nitrogen (N_2) in an AJA International ATC 2200-V load-locked turbo pumped sputtering system. A p-silicon (boron doped, $5 \times 10^{19}\ cm^{-3}$) substrate with <100> orientation was cleaned thoroughly with hydrofluoric acid (HF) to remove the native oxide. Additionally, the samples were sonicated in acetone, methanol, and isopropanol to remove organic materials on the surface of the substrate. The substrate was then loaded into the load lock and transferred to the main sputtering chamber with vacuum pressure of around 5×10^{-8} Torr. To ensure minimal contaminants in the TiN film, the chamber was outgassed before sputtering by raising the temperature to 800 °C while sputtering Ti as a getter material for a half hour. During the outgassing, the Si substrate was covered with an internal shutter. Immediately before sputtering, 40 sccm argon (Ar) gas was introduced into the system and a DC bias of 200 V was applied to the Si substrate for 5 minutes to clean its surface from any residual oxide. The Ar flow rate was then reduced to 12 sccm and N_2 was introduced to the chamber with a flow rate of 8 sccm. Maintaining this ratio of gases for the entire process, Ti was sputtered from an RF target for six hours while keeping the temperature at 700 °C, the substrate bias at 200 V, and the chamber pressure at 25 mTorr, resulting in 80 nm of TiN thin film deposited on silicon (Si). Similar sputtering steps were followed to deposit 80 nm of metallic TiN on a <100> MgO substrate at 650 °C and 120 V substrate bias. The only difference was in the ratio of Ar:N_2 which was 12:4 instead of 12:8 in the case of Si substrate.

A Woollam WVASE32 vertical angle spectroscopic ellipsometer (J.A. Woollam Company, Inc.) was used to characterize the optical properties of the TiN thin films. The ellipsometer has a Xenon (Xe) arc lamp as the excitation source within the range of 193 nm to 1700 nm with a collimated beam spot of 3 mm in diameter. Si and Indium Gallium Arsenide (InGaAs) detectors

covered the range from 185 to 1100 nm and 800 to 1700 nm respectively. The measurements were taken at three different incidence angles of 55°, 65°, and 75°. Figure S1 below compares the optical properties and FOM of our TiN thin films to those of Au thin films from different references.

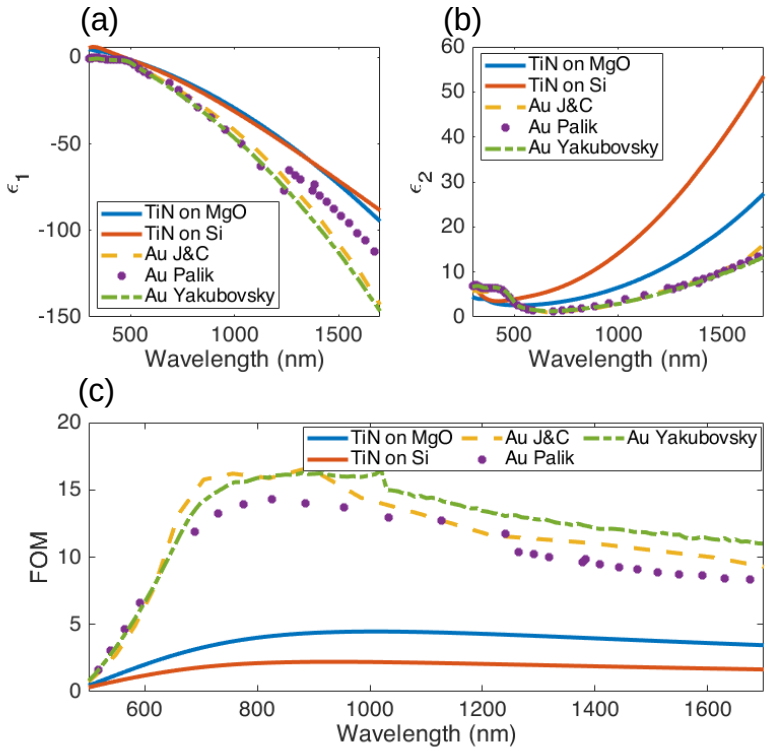

Figure S1: (a) Real and (b) Imaginary part of the dielectric function of Au obtained from Johnson and Christy[1], Palik[2], and Yakubivsky[3] and of our sputtered TiN thin films on Si and MgO substrates. (c) Comparison of the FOM of TiN and different Au thin films.

2. Design and Simulations

3D FDTD simulations were undertaken using the Lumerical software package with the appropriate boundary conditions (BC). To simulate an infinite array of nano-antennas in the *x* and *y* directions, the sidewalls of the computational domain were set to periodic BC. To allow for optimization and design flexibility, the distance between the sidewalls and the bowtie antenna were parametrized as $\frac{P_x}{2}$ and $\frac{P_y}{2}$ and the antenna arm horizontal height itself was parameterized as *h*. Initial optimization of the different antenna arrays designs was implemented using Particle Swarm Optimization (PSO)

to produce the maximum far field reflection at a specific resonant frequency. The particle swarm optimization (PSO) algorithm reduces the parameter space of geometrical parameter values (the length of the equilateral nano-bowties (h) and arrays' inter-element spacing (P_x, P_y), identifying an initial range of values. The PSO can search for either maxima or minima of a certain cost function or a figure of merit (in our case, the Far field reflection).

For each material system, we fed the PSO with the same range of values for the geometrical parameters (50nm$\leq P_x \leq$ one wavelength, 50nm$\leq P_y \leq$ one wavelength, 100nm$\leq h \leq$ one wavelength). As explained in[4] (a robust review on using PSO in electromagnetism), the algorithm starts the first iteration at a random value for (h, P_x, P_y) from the range specified by the user and keeps searching for different values of the geometrical parameters to find the first local maximum for the reflection (first better position called personal best1). The algorithm then explores another random value from the input and searches for another better position (higher maximum called personal best2). By comparing personal best1 to personal best2, the algorithm defines global best. PSO keeps updating the global best until it converges to a global maximum.

Similar to most of the optimization algorithms, PSO is not guaranteed to converge to the global optimal solution. Consequently, in order for us to refine the values we obtained from the PSO, we decided to run a greedy search algorithm using nested parameter sweep where the output of the PSO is used as the first initial guess (midpoint of our sweep values). This technique is efficient since our parameter space is not large (only three parameters). Moreover, we used two symmetry planes to reduce the computational cost by a factor of 4.

The TiN optical properties (Figure 1 in the manuscript) were imported to Lumerical and analytical multi-coefficient models (MCMs) were used to fit and extrapolate the experimental data and

ensure the stability of the computations. To simulate our FTIR experiments that use an unpolarized source, the simulations were run twice with two orthogonal polarizations, the first with P-polarization (E-field is perpendicular to the antenna's axis), and the second with S-polarization (E-field is parallel to the antenna's axis). The result was calculated as the average of these two simulations. The simulation model was then used to find the optimal dimensions of the nano-antennas and the spacing between the array elements to maximize the plasmonic coupling and produce far field reflection peaks and near field intensity enhancement in the cases of TiN on Si, TiN on MgO, Au on Si, and Au on MgO at different resonance wavelengths.

3. Fabrication

Au antennas on Si or MgO were formed by lift-off patterning of the Au, defined by e-beam written patterns. PMMA 495-C6, an e-beam resist, was applied to the substrate at 4,000 RPM for 45 seconds to give a resist thickness of around 600 nm. The sample was subsequently baked at 180 °C for 5 minutes. Elionix ELS-F125 125 keV e-beam lithography system was used with a beam current of 200 pA, field size of 100 μm, 50,000 dots, and exposure dose between 1,600 to 1,700 $\frac{\mu C}{cm^2}$. Electron beam evaporation (EE) was used to deposit 5 nm of chromium and 75 nm of Au. The sample was left in Acetone for overnight lift off.

TiN antennas on Si were formed by patterning the thin film and subsequent etching of the bow-tie patterns. We used the negative e-beam resist HSQ spun on top of the TiN thin film on Si at 3,000 RPM for 45 seconds to give a resist of around 600 nm in thickness. The sample was then baked at 180 °C for 5 minutes. To avoid cracking of the resist when brought from 180 °C to room temperature, we transferred the sample to another hot plate at 120 °C for 5 minutes before the sample was ready for exposure. The Elionix ELS-F125 e-beam lithography system was used with

a beam current of 1 nA, field size of 100 μm, 200,000 dots, and exposure dose between 1,000 to 2,000 $\frac{\mu C}{cm^2}$. Subsequent to exposure, the sample was developed in 25% Tetramethylammonium hydroxide (TMAH) for one minute and then rinsed using DI water to stop the development process. After development, HSQ transforms into SiO_2 and is used as a mask to transfer the pattern to the TiN film underneath through dry etching. This SiO_2 mask can then be removed by dipping the sample in HF for a few minutes. The preceding process is not suitable for patterning TiN antennas on MgO substrate, as HF etches the MgO substrate. Consequently, we used a different resist: ma-N 2410 by MicroChem, Inc. The resist was spun on at 4,000 RPM for 45 seconds, then baked at 90 °C for one minute. The same Elionix system was used with beam current of 1 nA, field size of 100 μm, 50,000 dots and exposure dose between 500 to 1,500 $\frac{\mu C}{cm^2}$. The sample was developed for one minute in AZ-726 metal ion free solution of 2.38% TMAH concentration and then immersed in DI water to stop the development process. The exact dose value for HSQ or ma-N depends on the size of the nano-structures and the film underneath the resist; therefore, a dose test array should always be performed to settle on the exact dose value. Beamer and Tracer software by GeniSys, Inc. were used to run Monte-Carlo simulation to correct for proximity effect errors caused by back-scattered electrons during electron beam exposure.

For both substrates (Si and MgO), a highly selective chlorine (Cl_2) based inductively coupled plasma reactive ion etching (ICP-RIE) process was used to transfer the pattern to the TiN thin film with plate bias of 80 V, ICP power of 400 W, pressure of 5 mTorr with Ar and Cl_2 flow rate of 84 sccm and 36 sccm respectively. Figure S2 shows a flow chart of the top-down fabrication steps and SEM images of Au and TiN nano-antennas on different substrates. Depending on the TiN film, the etch rate of our recipe at room temperature varies between 3.5 nm/second to 5 nm/second. The etch rates of TiN, Si, and MgO were characterized using atomic force microscopy

(AFM), showing a selectivity for TiN to Si of 2 to 1 and selectivity for TiN to MgO of 5 to 1. This selective etching process is highly controllable and can be stopped right at the surface of the substrate (Figure S2e). Both HSQ and ma-N 2410 exhibit minimal thickness reduction during the chlorine based RIE process. After etching, the HSQ-Fox16 mask was removed using HF and the ma-N 2410 mask was removed by soaking the sample in 25% TMAH for 24 hours. A post etch cleaning process was implemented using EKC-265 solution[5] at 70 °C for 20 minutes to remove possible resist residues, resulting from cross-linking of the resist in the plasma or sputter-deposition of substrate materials onto the resist.

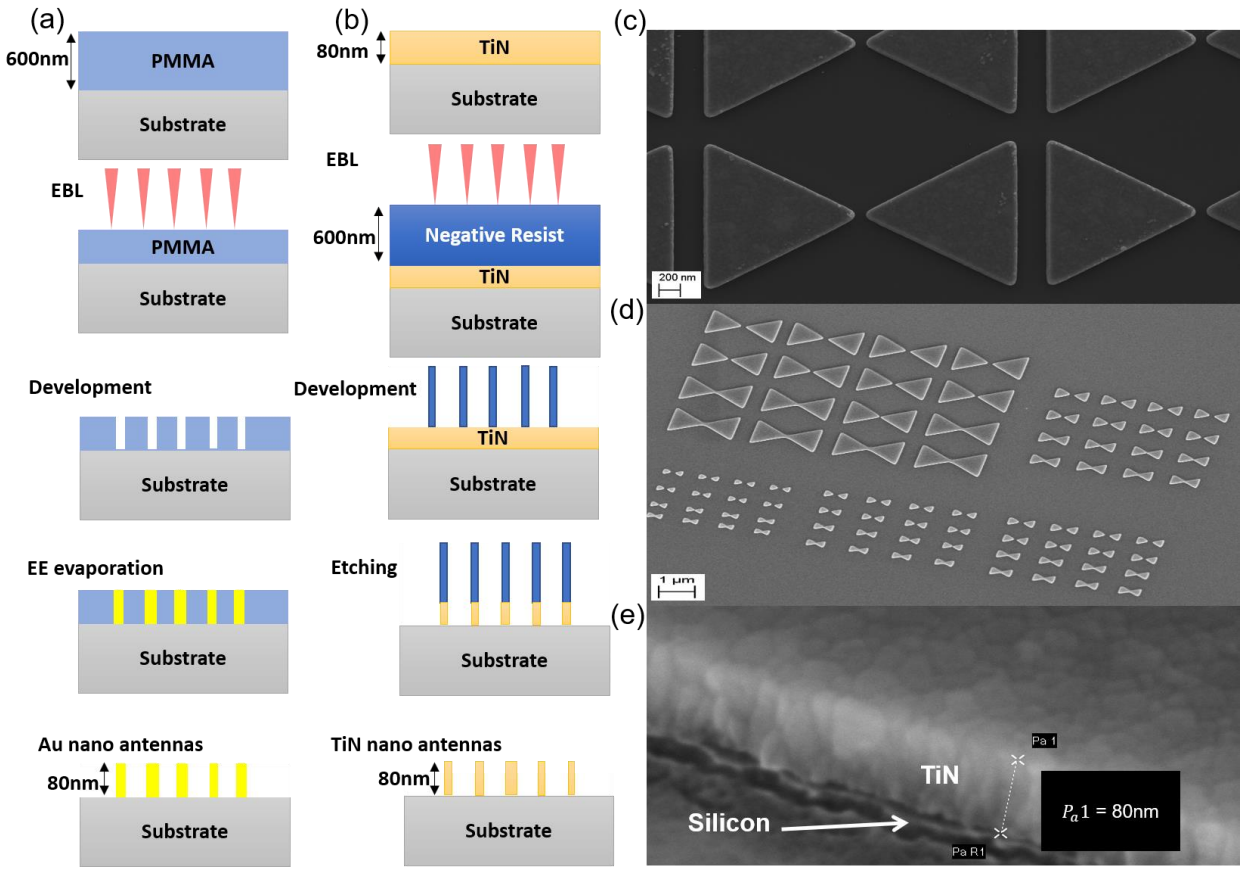

*Figure S2: T*op-down fabrication process flow for nano-antennas made of (a) Au and (b) TiN. (c) SEM image of Au bowtie nano-antenna array on Si substrate. (d) SEM image of TiN bowtie nano-antenna array on Si substrate. (e) 45° tilted SEM image of an 80 nm thick TiN nano-antenna on silicon showing the controllability of the etch process.

4. FTIR Measurements

The Fourier Transform Infrared (FTIR) Spectrometer uses a broadband light source made of silicon carbide (SiC). When heated with an electric current passing through it, the SiC source emits IR radiation with the characteristic spectrum following the black body radiation. A Michelson interferometer setup is used to generate an interferogram which can be converted into a reflection spectrum through Fourier Transform. In this setup, the beam is split by a beam splitter into two optical paths ending with one fixed mirror and one moving mirror which both send the light back to interfere at the beam splitter. The moving mirror scans back and forth changing the path length differences between the two arms of the Michelson interferometer so that different wavelengths interfere either constructively or destructively. The recombined beam at the beam splitter is then sent to the sample and the reflectance from the sample surface is measured by a mercury cadmium telluride detector with high signal to noise ratio. Because the detector can be triggered by thermal radiation, we kept the detector cooled using liquid nitrogen to minimize thermally induced noise and leakage currents. Background measurements were performed using a gold mirror with no sample present for correction of intensity differences at various wavelengths. The background measurements were also carried out for atmospheric compensation due to contributions of the water vapor and carbon dioxide absorbance in the atmosphere with the latter having two distinct peaks at around 4.3 μm.

Arrays of bow-tie antennas were fabricated to be 10 μm bigger than the spot size of the FTIR to act as an infinite array of plasmonic nano-antennas and match the simulations with periodic boundary conditions. During the FTIR measurements, it is usually the case that the incident power on the nano-antennas is either reflected, absorbed, or transmitted coherently. However, sometimes there exist diffuse reflections or scatterings that are wavelength independent.

We observed this phenomenon in our data, after background correction, as a baseline offset in the reflection spectra. To overcome this issue, we performed baseline corrections through fitting a polynomial curve to the baseline and then subtracting the baseline offset from the data to produce flat reflection curves. The baseline subtraction was around 10% to 20%. Figure S3 shows the FTIR results of TiN and Au nano-antennas on MgO substrate. As in the case of Si substrate, we witnessed a close resemblance between the FTIR reflection spectra from the Au and TiN on MgO. Although the nano-antennas on MgO substrate exhibit a similar plasmonic performance to those on Si, they produced better FTIR peaks (i.e., narrow band peaks with high off-resonance to on-resonance reflection ratio). This is because the resonant polarizability factor of the scattering cross section (ratio between the incident and the scattered radiation) increases with lower refractive index substrates and lower negative values of the real part of ε.[6-7] Consequently, although TiN on Si and TiN on MgO have similar negative values of the real part ε, the difference in their plasmonic performance can be attributed to two factors: 1) the higher refractive index of the Si substrate (3.4), which is about two times that of MgO (1.6), and 2) the larger Im(ε) for TiN on Si compared to that of TiN on MgO, indicating that TiN on Si is more lossy and thus shows weaker plasmonic peaks compared to TiN on MgO. On the other hand, the optical properties of Au films formed here are generally insensitive to the underlying substrate. Thus, the Au on MgO antennas show a better plasmonic coupling than Au on Si substrate, primarily due to the difference in the refractive index of the underlying substrate. The close resemblance between the FTIR reflection spectra from the Au and TiN on different substrates confirms that TiN can be used as a high quality refractory plasmonic material instead of Au regardless of the type of the substrate.

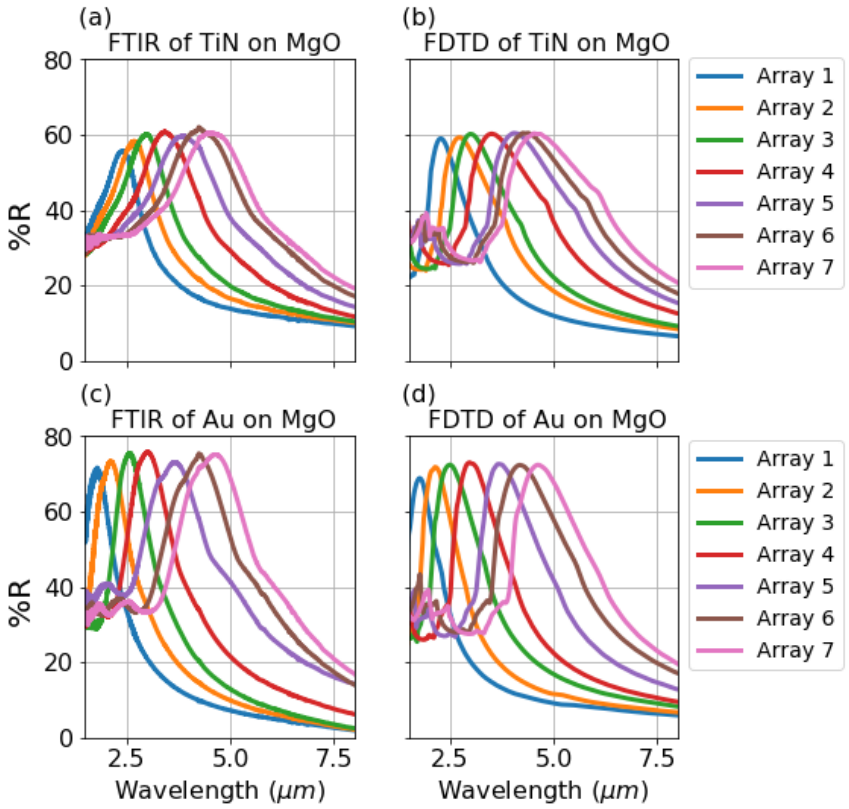

Figure S3. Matching experimental and simulated FTIR spectra from seven geometrically different nano-antenna arrays made of (a,b) TiN and (c,d) Au on MgO substrate. Each array exhibits a distinct plasmonic resonance highlighting the similarities between nano-structures made of Au and TiN in supporting highly tunable resonant enhanced scattering plasmonic peaks. h ranges from 300 nm in array 1 to 1000 nm in array 7 with a step of 100 nm. P_x and P_y range from 80 nm in array 1 to 240 nm in array 7.

5. XPS:

The XPS data were collected in an ultra-high vacuum chamber with base pressure at around 5×10^{-8} mBar, using Thermo-Scientific K-Alpha+ XPS. The instrument has a digitally-controlled monatomic argon ion sputtering gun with beam energy of 2 keV to carry out depth profiling. High-resolution survey scans were collected using a 180° double focusing hemispherical analyzer-128-channel detector with a monochromatic micro-focused Al K-alpha as a primary excitation source with spot size of 400 microns. The XPS data presented in Figure S4 show the effect of annealing on the composition of the TiN thin film through a depth profile analysis. During the experiment, Ar was used to etch a few nanometers into the thin film and at every etch step the film composition was measured. At room temperature and 400 °C (Figure S4a and S4b), the film

shows a very similar composition of titanium, nitrogen, and oxygen with the same ratios, thus the very similar plasmonic response as shown in Figure 4a in the manuscript. (Note: For room temperature and 400 °C annealed films, we do not etch down to the substrate as the films are expected to be quite uniform in chemical composition away from the surface of the sample). The percentage of oxygen increases substantially for the 600 °C annealed TiN film, suggesting a surface layer (10 nm) of titanium oxide (Figure S4c). Below the oxide, the bulk of the film composition converged to the room temperature and 400 °C composition with very similar elemental ratios. This 10 nm of titanium oxide formation can explain the slight shift in the FTIR curve of TiN nano-antennas and the change in color of the TiN thin film annealed at 600 °C (insets of Figure 4c in the manuscript). This experimental observation was further confirmed by the FDTD simulations presented in Figure S5 showing a red shift in the plasmonic resonance due to the formation of 10 nm oxide layer on the surface of a TiN nano-antenna. Additionally, the SEM images presented in the insets of Figures S4a, S4b, and S4c show a very similar microscopic appearance of the TiN thin films' cross sections.

Annealing at 800 °C, on the other hand, results in the compositional profile shown in Figure S4d where the XPS spectrum shows almost full conversion of the film from metallic titanium nitride to titanium oxide with an insignificant amount of nitrogen content in the film. The nearly complete oxidation of the film substantially reduces its plasmonic performance, as shown by the red curve in the FTIR spectrum in Figure 4a in the manuscript. This is also noticeable when comparing the microscopic appearance of the cross section of the TiN thin film annealed at 800 °C (inset of Figure S4d) to those annealed at lower temperatures (insets of Figures S4a, S4b and S4c). These observations about the dynamics of TiN oxidation at high temperatures agree with the literature.[8]

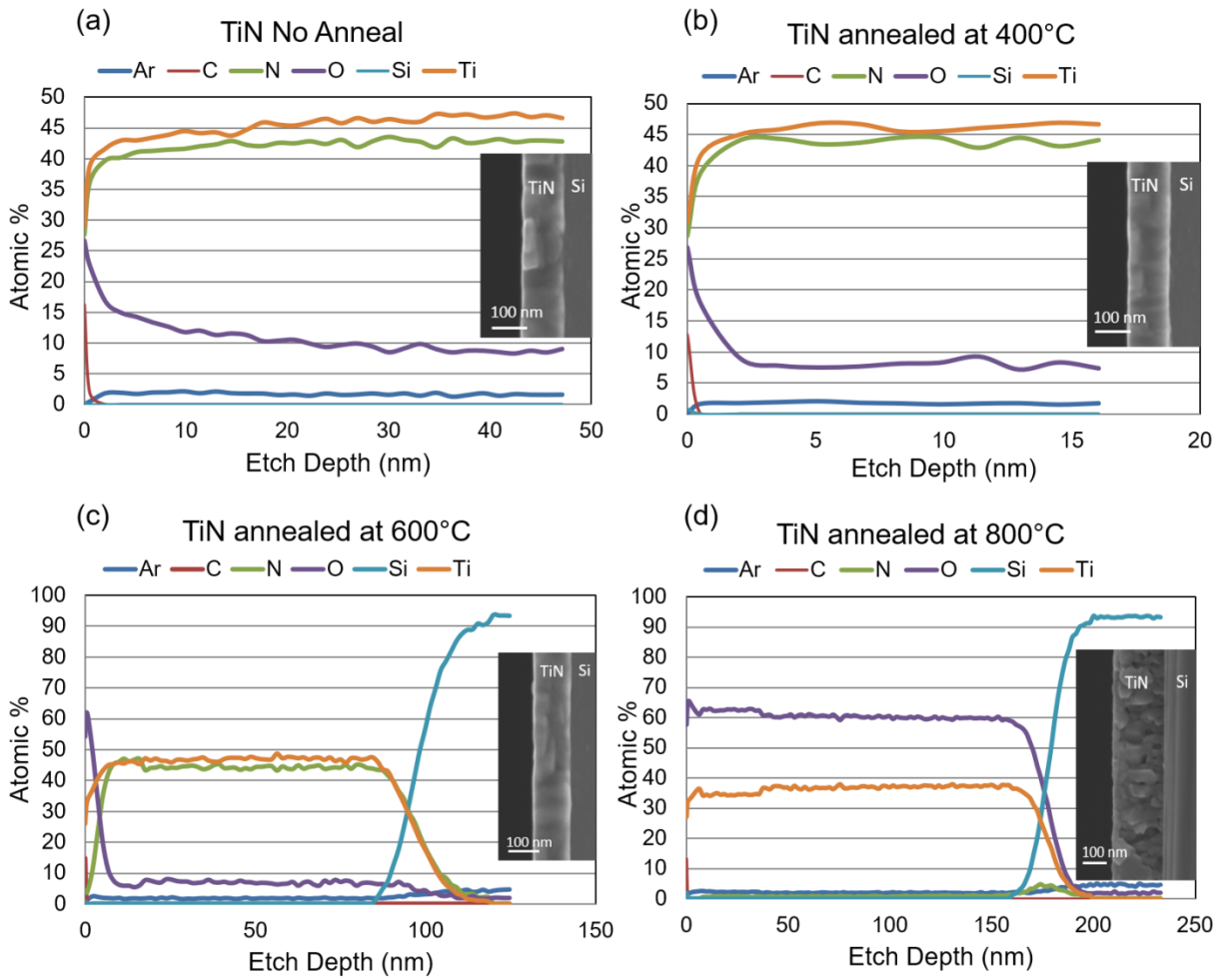

Figure S4. XPS spectra depth profile showing the chemical composition of the surface and the bulk of TiN thin films annealed at different temperatures. (a) Unannealed and (b) annealed at 400 °C samples have about the same bulk chemical composition below the surface. (c) The film annealed at 600 °C forms a thin oxide layer ~10 nm thick, below which the TiN composition is very similar to the room temperature and 400 °C annealed sample. (d) The film annealed at 800 °C is completely oxidized. The high temperature annealing in air and subsequent change in composition of the TiN films provides good correlation with the curves shown in Figure 4a in the manuscript. The insets show an SEM image of the TiN thin film cross section after every annealing step.

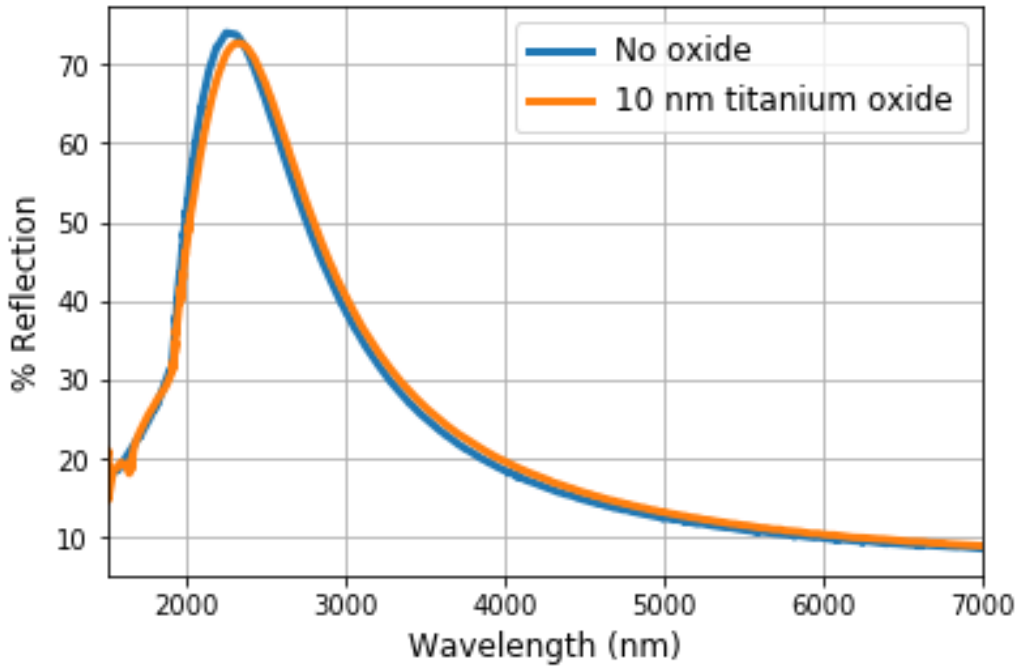

Figure S5: FDTD simulations showing the effect of creation of 10 nm titanium dioxide on the plasmonic resonance of TiN nano-antennas.

There exist different reports in the literature[8-19] that discuss the oxidation kinetics of TiN thin films (different activation time, different annealing temperatures and ramping conditions and different annealing time needed for complete oxidation) and how the oxidation behavior relates to the deposition conditions. The results from these reports are very different and appear to be contradictory. This is because the rate of the oxidation process depends on not only the annealing protocol but, more importantly, crystallinity, grain size, grain boundaries and the stoichiometry of the film. Therefore, it is worth mentioning that the oxidation kinetics we observe through our XPS analysis are very particular to our TiN thin film and our annealing protocol (10 minutes of annealing after the furnace equilibrates at the desired temperature). Although studying the maximum cycling temperature and potential longevity at elevated temperatures for TiN and Au is an important research topic, it is outside the scope of this paper. We are mainly concerned with the short annealing period after which the Au plasmonic performance becomes unstable compared

to that of TiN. Consequently, we used the changes in the optical response as the most suitable metric to directly compare the effect of annealing on the plasmonic response TiN and Au nanostructures. This is particularly important for thermo-plasmonic applications such as cancer treatment[20-21] and photothermal-imaging[22] that uses ultra-short pulse lasers and induce significant local temperature gradient but for a very short period of time. For these applications, our TiN thin film can be an excellent plasmonic material alternative to Au.

6. S-SNOM:

In order to find the exact dimensions that maximizes the near field intensity for a 6 μm illumination source, we ran FDTD simulations to compute the local field intensity enhancement spectrum 50 nm on top of the nano gap between the bowtie arms. Figure S6 compares the variation of the maximum near field intensity enhancement resonance wavelength with the antenna arm height (*h*) for both TiN and Au isolated bowtie nano-antennas on MgO. As Figure S6 indicates, the near field intensity enhancement value and spectral location for both TiN and Au are very similar, and the maximum near field intensity enhancement due to the local surface plasmon (LSP) resonance for 6 μm excitation occurs at a resonant bowtie arm length of 1.6 μm for both materials. On the other hand, for TiN and Au on Si the maximum LSP resonance height is 0.7 μm. This is to be expected since the LSP resonance blue shifts with lower refractive index substrates. Additionally, the lower refractive index substrates is expected to enhance the LSP resonance through the maximization of the polarizability factor.[7]

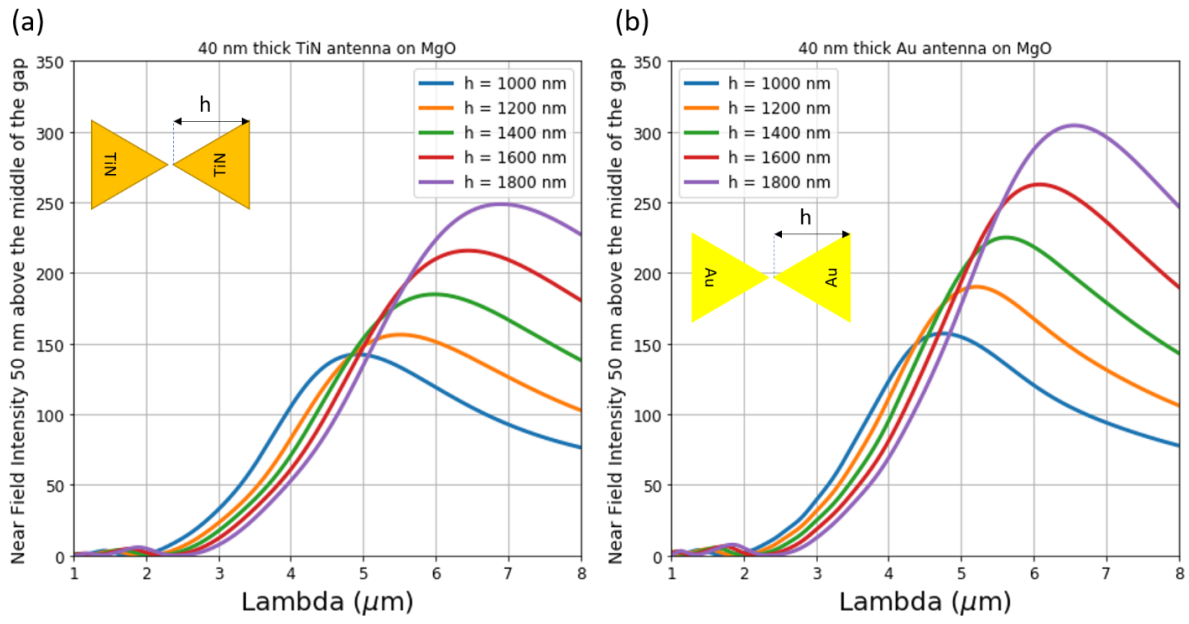

Figure S6. Comparison of optical near field intensity enhancement on top of the 50 nm gap for (a) TiN and (b) Au nano-antenna on MgO substrate showing the similarity between the near field enhancement capabilities of both Au and TiN nano-antennas and the dependence of the near field resonance wavelength on the antenna dimensions. The insets show the simulated geometry.

Figure S7 and Figure S8 present experimental and simulation results for the magnitude, phase, real and imaginary representation of the LSP modes for TiN and Au bow-tie nano-antennas on MgO and Si substrate respectively. For MgO (Figure S7) or Si (Figure S8) substrates, TiN and Au nano-antennas show very similar near field distributions with a strong dipolar LSP mode for the antennas with the resonant dimensions according to Figure S6. In order to validate that this is a resonance phenomenon, we fabricated and analyzed off-resonance antennas. For the MgO substrate, we fabricated isolated bowtie nano-antennas in both TiN and Au that are 0.5 μm shorter than the resonance antenna height for 6 μm illumination. For the Si substrate, we fabricated isolated bow-tie nano-antennas in TiN and Au that are 0.8 μm taller than the resonance antenna height for 6 μm illumination. Figure S9 and Figure S10 present experimental and simulation results for the magnitude, phase, real and imaginary representation of the weakly coupled localized surface plasmons for off-resonance TiN and Au bow-tie nano-antennas on MgO and Si substrate

respectively. This data shows a significant drop in the coupling intensity between the excitation source and the LSP modes and consequently the value of the near field intensity enhancement. This can also be seen in the LSP spatial distribution on the surface of the off-resonance antenna on Si substrate (Figure S10) where we do not observe a dipolar mode distribution in the real part of the near field.

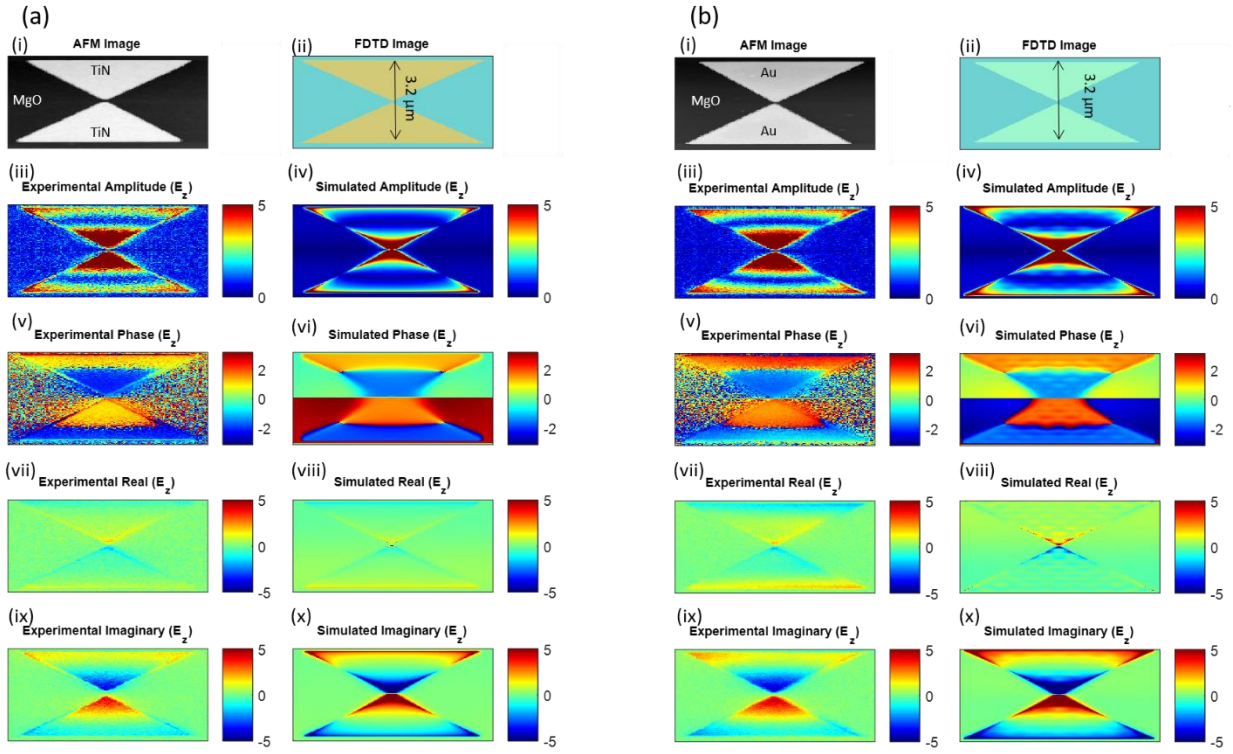

Figure S7. Resonant LSP modes in (a) TiN and (b) Au nano-antenna on MgO substrate showing the strong interaction between the exciting electromagnetic waves and the nanostructures. (i) AFM Topography of 3.2 µm long (a-i) TiN and (b-i) Au bow-tie nanoantenna on MgO. (ii) Simulated (a-ii) TiN and (b-ii) Au antenna in FDTD with E-field polarization parallel to the antenna axis with optical properties adapted from Figure 1. (iii) S-SNOM measured amplitude of the out of plane E-field component on the surface of the (a-iii) TiN and (b-iii) Au antenna. (v) S-SNOM measured phase heat map of (a-v) TiN and (b-v) Au nano-antenna ranging from $-\pi$ to π showing a strong dipolar bright mode evident in the 180^{o} phase shift across the gap. S-SNOM measured (vii) Real and (ix) Imaginary components of the localized surface plasmon in (a) TiN and (b) Au nano-antenna showing a strong dipolar distribution. (iv, vi, viii, x) FDTD simulations of the S-SNOM measurements for (iv) amplitude, (vi) phase (viii) real, and (x) imaginary part of (a) TiN and (b) Au nano-antenna showing excellent agreement with the measurements.

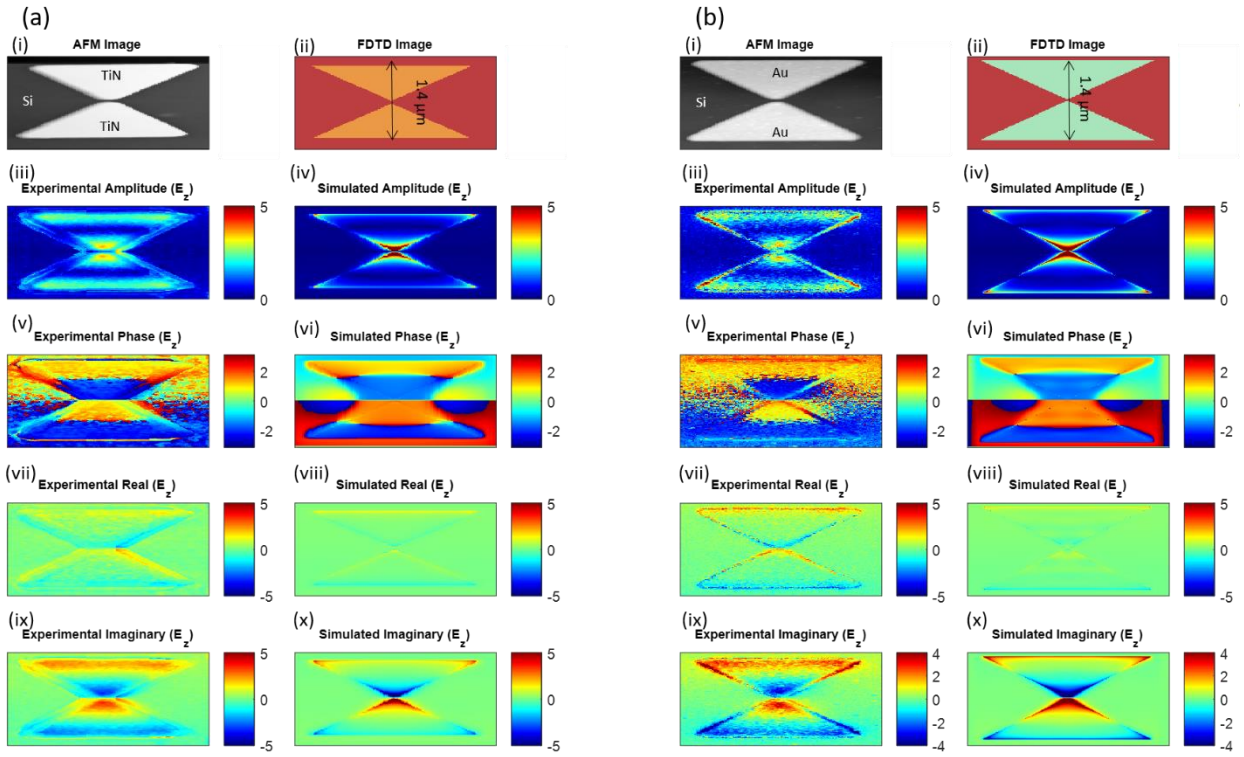

Figure S8. Resonant LSP modes in (a) TiN and (b) Au nano-antenna on Si substrate showing the strong interaction between the exciting electromagnetic waves and the nanostructures. (i) AFM Topography of 1.4 µm long (a-i) TiN and (b-i) Au bow-tie nanoantenna on Si. (ii) Simulated (a-ii) TiN and (b-ii) Au antenna in FDTD with E-field polarization parallel to the antenna axis with optical properties adapted from Figure 1. (iii) S-SNOM measured amplitude of the out of plane E-field component on the surface of the (a-iii) TiN and (b-iii) Au antenna. (v) S-SNOM measured phase heat map of (a-v) TiN and (b-v) Au nano-antenna ranging from $-\pi$ to π showing a strong dipolar bright mode evident in the 180^{o} phase shift across the gap. S-SNOM measured (vii) Real and (ix) Imaginary components of the localized surface plasmon in (a) TiN and (b) Au nano-antenna showing a strong dipolar distribution. (iv, vi, viii, x) FDTD simulations of the S-SNOM measurements for (iv) amplitude, (vi) phase (viii) real, and (x) imaginary part of (a) TiN and (b) Au nano-antenna showing excellent agreement with the measurements.

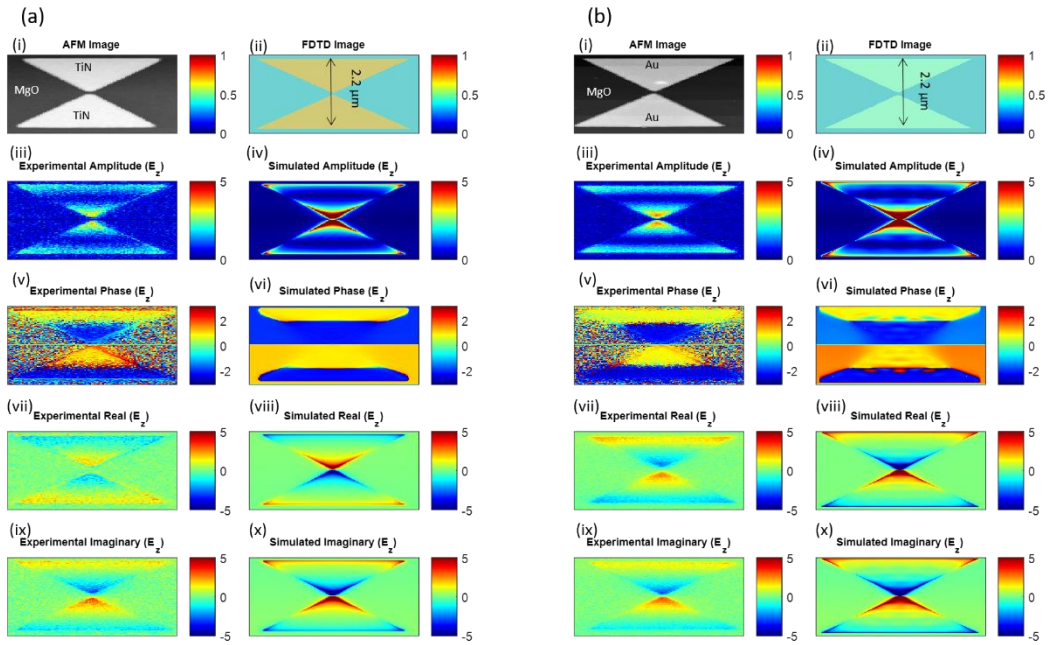

Figure S9. Off-resonant LSP modes in (a) TiN and (b) Au nano-antenna on MgO substrate showing weak interaction between the exciting electromagnetic waves and the nanostructures. (i) AFM Topography of 1.4 μm long (a-i) TiN and (b-i) Au bow-tie nanoantenna on MgO. (ii) Simulated (a-ii) TiN and (b-ii) Au antenna in FDTD with E-field polarization parallel to the antenna axis with optical properties adapted from Figure 1. (iii) S-SNOM measured amplitude of the out of plane E-field component on the surface of the (a-iii) TiN and (b-iii) Au antenna. (v) S-SNOM measured phase heat map of (a-v) TiN and (b-v) Au nano-antenna ranging from $-\pi$ to π showing a weak dipolar bright mode evident in the 180^{o} phase shift across the gap. S-SNOM measured (vii) Real and (ix) Imaginary components of the localized surface plasmon in (a) TiN and (b) Au nano-antenna showing a strong dipolar distribution. (iv, vi, viii, x) FDTD simulations of the S-SNOM measurements for (iv) amplitude, (vi) phase (viii) real, and (x) imaginary part of (a) TiN and (b) Au nano-antenna showing excellent agreement with the measurements.

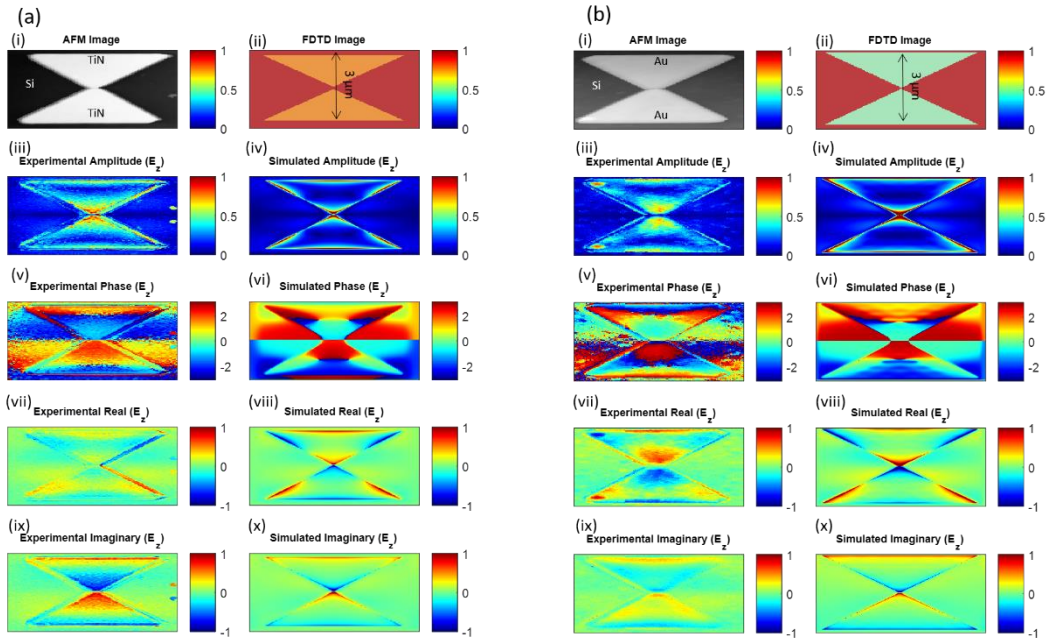

Figure S10. Off-resonant LSP modes in (a) TiN and (b) Au nano-antenna on Si substrate showing the strong interaction between the exciting electromagnetic waves and the nanostructures. (i) AFM Topography of 1.4 μm long (a-i) TiN and (b-i) Au bow-tie nanoantenna on Si. (ii) Simulated (a-ii) TiN and (b-ii) Au antenna in FDTD with E-field polarization parallel to the antenna axis with optical properties adapted from Figure 1. (iii) S-SNOM measured amplitude of the out of plane E-field component on the surface of the (a-iii) TiN and (b-iii) Au antenna. (v) S-SNOM measured phase heat map of (a-v) TiN and (b-v) Au nano-antenna ranging from $-\pi$ to π showing a weak nondipolar bright mode evident in the 180^{o} phase shift across the gap. S-SNOM measured (vii) Real and (ix) Imaginary components of the localized surface plasmon in (a) TiN and (b) Au nano-antenna showing a strong dipolar distribution. (iv, vi, viii, x) FDTD simulations of the S-SNOM measurements for (iv) amplitude, (vi) phase (viii) real, and (x) imaginary part of (a) TiN and (b) Au nano-antenna showing excellent agreement with the measurements.

REFERENCES

1. Johnson, P. B.; Christy, R.-W., Optical Constants of the Noble Metals. *Physical review B* **1972,** *6* (12), 4370.
2. Palik, E. D., *Handbook of Optical Constants of Solids*. Academic press: 1998; Vol. 3.
3. Yakubovsky, D. I.; Arsenin, A. V.; Stebunov, Y. V.; Fedyanin, D. Y.; Volkov, V. S., Optical Constants and Structural Properties of Thin Gold Films. *Optics express* **2017,** *25* (21), 25574-25587.
4. Robinson, J.; Rahmat-Samii, Y., Particle Swarm Optimization in Electromagnetics. *IEEE transactions on antennas and propagation* **2004,** *52* (2), 397-407.
5. http://www.dupont.com/content/dam/dupont/products-and-services/electronic-and-electrical-materials/documents/ekc/EKC265.pdf.
6. Bohren, C. F.; Huffman, D. R., *Absorption and Scattering of Light by Small Particles*. John Wiley & Sons: 2008.
7. Kuwata, H.; Tamaru, H.; Esumi, K.; Miyano, K., Resonant Light Scattering from Metal Nanoparticles: Practical Analysis Beyond Rayleigh Approximation. *Applied physics letters* **2003,** *83* (22), 4625-4627.
8. Chen, H.-Y.; Lu, F.-H., Oxidation Behavior of Titanium Nitride Films. *Journal of Vacuum Science & Technology A: Vacuum, Surfaces, and Films* **2005,** *23* (4), 1006-1009.

9. Briggs, J. A.; Naik, G. V.; Zhao, Y.; Petach, T. A.; Sahasrabuddhe, K.; Goldhaber-Gordon, D.; Melosh, N. A.; Dionne, J. A., Temperature-Dependent Optical Properties of Titanium Nitride. *Applied Physics Letters* **2017,** *110* (10), 101901.
10. Esaka, F.; Furuya, K.; Shimada, H.; Imamura, M.; Matsubayashi, N.; Sato, H.; Nishijima, A.; Kawana, A.; Ichimura, H.; Kikuchi, T., Comparison of Surface Oxidation of Titanium Nitride and Chromium Nitride Films Studied by X-Ray Absorption and Photoelectron Spectroscopy. *Journal of Vacuum Science & Technology A: Vacuum, Surfaces, and Films* **1997,** *15* (5), 2521-2528.
11. Wells, M. P.; Bower, R.; Kilmurray, R.; Zou, B.; Mihai, A. P.; Gobalakrichenane, G.; Alford, N. M.; Oulton, R. F.; Cohen, L. F.; Maier, S. A., Temperature Stability of Thin Film Refractory Plasmonic Materials. *Optics express* **2018,** *26* (12), 15726-15744.
12. Gautier, S.; Komninou, P.; Patsalas, P.; Kehagias, T.; Logothetidis, S.; Dimitriadis, C.; Nouet, G., Optical and Electrical Properties of Tin/N-Gan Contacts in Correlation with Their Structural Properties. *Semiconductor science and technology* **2003,** *18* (6), 594.
13. Desmaison, J.; Lefort, P.; Billy, M., Oxidation Mechanism of Titanium Nitride in Oxygen. *Oxidation of Metals* **1979,** *13* (6), 505-517.
14. Logothetidis, S.; Meletis, E.; Stergioudis, G.; Adjaottor, A., Room Temperature Oxidation Behavior of Tin Thin Films. *Thin Solid Films* **1999,** *338* (1-2), 304-313.
15. Tompkins, H. G., The Initial Stages of the Oxidation of Titanium Nitride. *Journal of Applied Physics* **1992,** *71* (2), 980-983.
16. Wittmer, M.; Noser, J.; Melchior, H., Oxidation Kinetics of Tin Thin Films. *Journal of Applied Physics* **1981,** *52* (11), 6659-6664.
17. Yin, Y.; Hang, L.; Zhang, S.; Bui, X., Thermal Oxidation Properties of Titanium Nitride and Titanium–Aluminum Nitride Materials—a Perspective for High Temperature Air-Stable Solar Selective Absorber Applications. *Thin Solid Films* **2007,** *515* (5), 2829-2832.
18. Wu, H.; Chou, T.; Mishra, A.; Anderson, D.; Lampert, J.; Gujrathi, S., Characterization of Titanium Nitride Thin Films. *Thin Solid Films* **1990,** *191* (1), 55-67.
19. Tompkins, H. G., Oxidation of Titanium Nitride in Room Air and in Dry O2. *Journal of Applied Physics* **1991,** *70* (7), 3876-3880.
20. Stern, J. M.; Stanfield, J.; Kabbani, W.; Hsieh, J.-T.; Cadeddu, J. A., Selective Prostate Cancer Thermal Ablation with Laser Activated Gold Nanoshells. *The Journal of urology* **2008,** *179* (2), 748-753.
21. Saklayen, N.; Huber, M.; Madrid, M.; Nuzzo, V.; Vulis, D. I.; Shen, W.; Nelson, J.; McClelland, A. A.; Heisterkamp, A.; Mazur, E., Intracellular Delivery Using Nanosecond-Laser Excitation of Large-Area Plasmonic Substrates. *ACS nano* **2017,** *11* (4), 3671-3680.
22. Gaiduk, A.; Ruijgrok, P. V.; Yorulmaz, M.; Orrit, M., Detection Limits in Photothermal Microscopy. *Chemical Science* **2010,** *1* (3), 343-350.